ORIGINAL PAPER

Photomagnetic hybrid ultrathin films

Takashi Yamamoto · Yasuaki Einaga

Abstract Two novel types of photomagnetic hybrid ultrathin film (film A and B) of metal cyanides have been fabricated by means of the modified Langmuir–Blodgett method using a smectite clay mineral. Film A is composed of an amphiphilic azobenzene cation, a montmorillonite, and Prussian Blue in which photocontrol in the magnetization was realized by the photoisomerization of azobenzene chromophore. The observed photomagnetic efficiency was large (ca. 11%) due to the well-organized structure of the ultrathin film. Film B is composed of a quaternary ammonium salt, a montmorillonite, and Co–Fe Prussian Blue in which the photoinduced magnetization caused by the electron transfer exhibited an anisotropic response with regards to the direction of the applied magnetic field. This phenomenon is ascribed to the unique structure of Co–Fe Prussian Blue formed onto the clay layer.

Keywords Photomagnet · Organic–inorganic hybrid · Langmuir–Blodgett films · Prussian Blue · Clay mineral

Introduction

Optically switchable magnetic materials are becoming increasingly important in the field of high-density information storage device, because the photon mode allows us to access a wide range of materials with high speed and superior resolution [1–3]. In particular, the design of molecular

T. Yamamoto · Y. Einaga (✉)
Department of Chemistry, Faculty of Science and Technology,
Keio University,
3-14-1 Hiyoshi,
Yokohama 223-8522, Japan
e-mail: einaga@chem.keio.ac.jp

compounds that exhibit photoinduced magnetization behavior has attracted great attention, and several molecular photomagnetic materials were developed [4–7]. They include, for example, cyanide-bridged metal complexes such as Prussian Blue (also its analogues) [8, 9] and crystalline metal-assembled complexes [10]. Although reversible photocontrol of magnetic properties or electronic states including spin states in these compounds was realized, most of such interesting phenomena were observed only at low temperature. Furthermore, the number of optically switchable molecular solids reported has been quite small. This is because the strategies that are necessary to achieve photoinduced magnetic switching in a solid state are yet to be clarified. In other words, it is desirable to propose a novel strategy for the development of photoswitchable magnetic materials. Along this line, we have focused on the incorporation of magnetic materials into photochromic assemblies to facilitate the photocontrol of magnetization: Prussian Blue formed in vesicles [11, 12], Langmuir–Blodgett (LB) films [13–15], or reverse micelles [16] and iron oxide nanoparticles enclosed by vesicles [17, 18], coordinated by ligands [19] or embedded in layer-by-layer films [20]. Our strategy has offered new perspectives for the photocontrollable magnetic materials, and a variety of hybrid photomagnets have been fabricated by this methodology [21–23].

Ultrathin films with highly ordered structures have many applications in the field of optical devices, microelectronic devices, and sensors [24–27]. From this viewpoint, when preparing the device consisting of photoswitchable magnetic materials, it is required to fabricate their ultrathin films with the control-assembled manner. In actual practice, up to now, the photomagnetic films have been mainly prepared by an electrochemical method [28–30]. However, with regards to the uniformity and orientation of the films, it would be an

inadequate fabrication methodology. Moreover, it would be difficult to control the film thickness on nanoscale and construct the hybrid films that consisted of more than one component. On the other hand, the Langmuir–Blodgett method is one of the most useful techniques for preparing ultrathin films in which the layer number and the sequence can be controlled at the molecular level [24, 25]. On the basis of this feature, metal cyanide extended networks, two-dimensional assemblies of Prussian Blue, have been fabricated as a part of LB films [31, 32]. Among a variety of the deposition methods, it is fascinating to use a clay mineral, so-called 'clay LB method' [33–35]. It is revealed that the hybrid ultrathin films prepared by this method possess some remarkable features: (1) The layered structure of the film is quite stable due to the existence of the rigid clay layers; (2) Cationic compounds can be intercalated into the hybrid film by an ion exchange reaction with the clay layer; and (3) The cations in the adsorbed layer are sandwiched in noncentrosymmetric fashion. Therefore, it would be effective to prepare functional ultrathin films by this modified LB method.

In this paper, we will describe two examples of the photoswitchable magnetic ultrathin films. One is composed of an azobenzene, a clay mineral, and Prussian Blue (film A) and the other is consists of an ammonium salt, a clay mineral, and Co–Fe Prussian Blue (film B). For film A, we could achieve photocontrol in magnetization with the large photomagnetic efficiency (ca. 11%). Moreover, such a photomagnetic film could be only prepared by our combined methodology represented in this manuscript. For film B, we could observe the so-called "anisotropic photoinduced magnetization effect", which has not been observed in the bulk. Therefore, the observation of such a phenomenon offers new perspectives on the utilization for the clay LB films, not only as a nanoscale object but also as an effective template in the fabrication of functional ultrathin films.

Materials and methods

Materials

Film A was composed of an azobenzene, {5-[4-(4-dodecyloxyphenylazo)phenoxy]pentyl}(2-hydroxyethyl)dimethyl ammonium bromide ($C_{12}AzoC_5N^+$; Fig. 1a), as the amphiphilic cation, montmorillonite (*Kunipia P*) as the clay mineral, and Prussian Blue as the magnetic material. $C_{12}AzoC_5N^+$ was synthesized according to a previous report [36]. $C_{12}AzoC_5N^+$ was dissolved in a 9:1 mixture (by volume) of dichloromethane and ethanol to prepare a solution at 2.7×10^{-3} M. Film B was composed of a quaternary ammonium salt, didodecyldimethylammonium bromide (DDAB; Fig. 1b) as the amphiphilic cation,
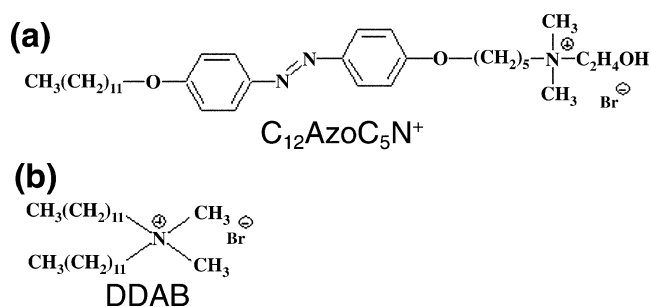
Fig. 1 Structure of amphiphiles: **a** $C_{12}AzoC_5N^{(+)}$ and **b** DDAB

montmorillonite (*Kunipia P*) as the clay mineral, and Co–Fe Prussian Blue as the photomagnetic material. DDAB purchased from Aldrich was used as received, and dissolved in chloroform to prepare a solution at 2.0×10^{-3} M.

The smectite clay mineral, *Kunipia P*, was purchased from Kunimine, Japan. The cation-exchange capacity of the clay was 1.074 mEq g^{-1}. The thickness of the clay single nanosheet, estimated from their crystal structure, was 9.6 Å [37]. The stock suspension of the clay was prepared by dispersing 1 g of the clay in 1,000 ml of pure water and diluting it to a given concentration with pure water just before use as a subphase.

$FeCl_2 \cdot 4H_2O$, $CoCl_2$, and $K_3[Fe(CN)_6]$ were purchased from WAKO Pure Chemicals and used without further purification. The water was purified with a Simpli Lab water system (Millipore) to a specific resistivity of 18.2 MΩ cm.

Substrate preparation

Glass plates were used as deposition substrates for UV–vis, infrared external reflection (IR-ER), X-ray diffraction (XRD), and X-ray photoelectron spectroscopy (XPS) measurements. A calcium fluoride (CaF_2) plate, purchased from Pier Optics, was used as deposition substrates for the Fourier transform infrared spectroscopy (FT-IR) measurements. Samples for superconducting quantum interference device (SQUID) measurement were prepared on a micro cover glass (thickness 0.12–0.17 mm) or Mylar (Teijin DuPont Films) substrates cleaned before use with absolute ethanol. All of the substrates were rendered hydrophobic by treating them with octadecyltriethoxysilane.

Film preparation

A schematic illustration of the ultrathin film preparation process is shown in Fig. 2. The solution of amphiphilic cations (film A $C_{12}AzoC_5N^+$ and film B DDAB) was spread on the subphase of the clay suspension (film A 50 mg l^{-1} and film B 90 mg l^{-1}) at room temperature. A floating monolayer of cations was hybridized with the clay single nanosheet at the air–suspension interface. Fifteen minutes later, hybrid monolayers were compressed up to a desired surface pressure (film
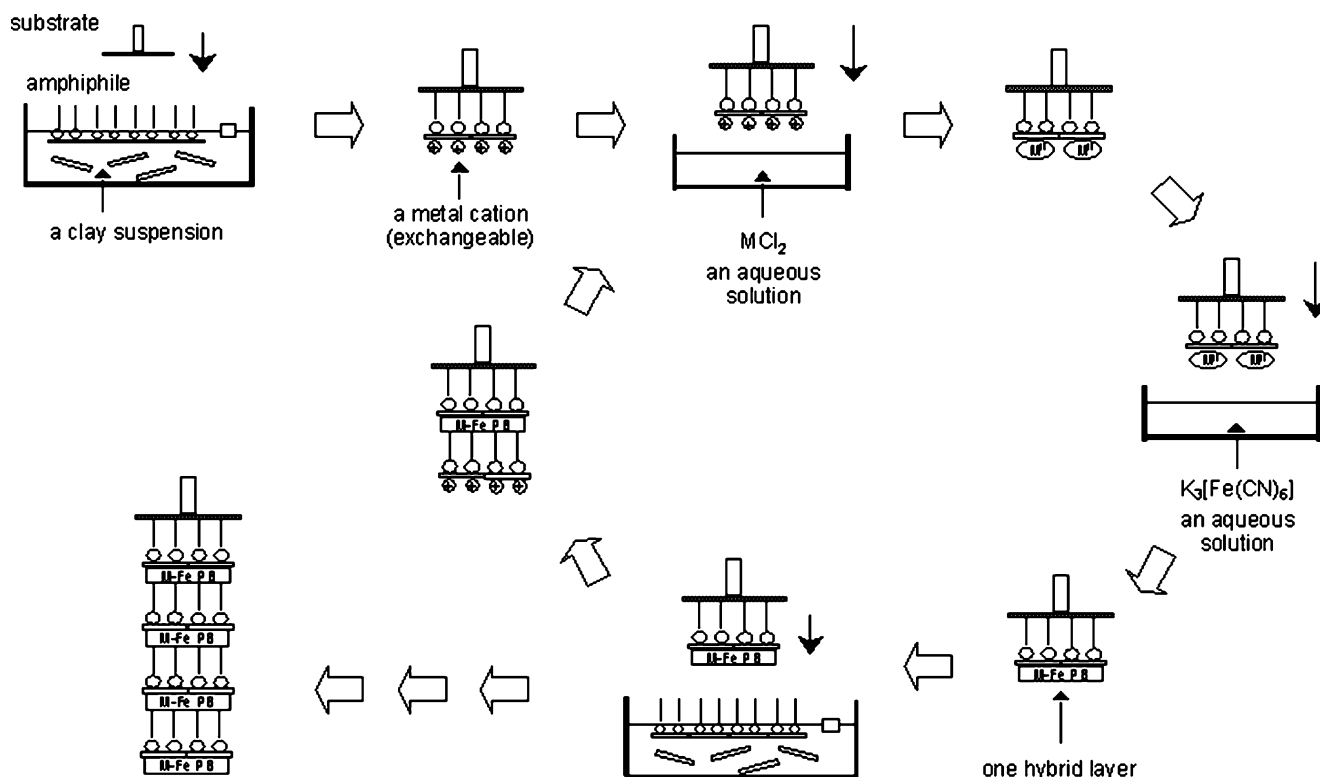
Fig. 2 A schematic illustration of the hybrid ultrathin films preparation method. Hybrid ultrathin films are composed of amphiphiles (film A, $C_{12}AzoC_5N^+$; film B, DDAB), clay single nanosheets, and M–Fe Prussian Blue (film A, M=Fe; film B, M=Co)

A 30 mN m^{-1} and film B 10 mN m^{-1}). After 35 min, floating hybrid monolayers were transferred as X-type film onto the hydrophobic surface of substrates by the horizontal dipping technique. The surface of the transferred film was rinsed with pure water several times and was then immersed in an aqueous $M^{II}Cl_2$ (film A $FeCl_2 \cdot 4H_2O$; film B $CoCl_2$) solution (10 mM) for 1 min to exchange the metal ions with the exchangeable metal ones. After rinsing the surface well with pure water again, it was dipped in an aqueous $K_3[Fe(CN)_6]$ (common to films A and B) solution (10 mM) for 1 min to form a metal cyanide layer (film A Prussian Blue; film B: Co–Fe Prussian Blue) on the surface of the hybrid film. The surface was rinsed well with pure water and dried by N_2 stream. Hybrid ultrathin films composed of the amphiphilic cations, the clay single nanosheets, and the metal cyanides were fabricated by repeating this procedure. One unit layer composed of the amphiphilic cations, the clay single nanosheets, and the metal cyanides is hereafter designated as one hybrid layer.

Instruments

The preparation of hybrid monolayers and measurements of the surface pressure–molecular area (π–A) isotherms were carried out using a computer-controlled film balance system, the FSD-50 (USI System). UV–vis and FT-IR absorption spectra were recorded on a V-560 spectropho-

tometer (JASCO) and a FT/IR-660Plus spectrometer (JASCO), respectively. UV–vis and FT-IR measurements at low temperature were performed with a closed-cycle helium refrigerator (Iwatani). UV illumination (filtered light, λ_{max}=360 nm, 1.0 mW cm^{-2}) was carried out using an ultrahigh pressure mercury lamp (HYPERCURE 200, Yamashita Denso). Visible light illumination (400–700 nm, 1 mW cm^{-2}) was similarly carried out using a xenon lamp (XFL-300, Yamashita Denso). IR-ER absorption spectra were recorded on a Spectrum One FT-IR spectrometer (Perkin Elmer) equipped with a variable angle specular reflectance accessory. XRD patterns were recorded on a Philips X'Pert MRD high resolution X-ray diffractometer using Ni-filtered CuKα radiation. The XPS spectra were obtained on an ESCA Model 1600 C-Type spectrometer (ULVAC-PHI) using the AlKα line source at 1486.6 eV. The magnetic properties were investigated with a superconducting quantum interference device magnetometer (Model MPMS-5S, Quantum Design).

Results and discussion

We refer to the characterization of two types of hybrid ultrathin film (i.e., films A and B). Therefore, the obtained results would be described in a separate manner.

Section for Film A (C$_{12}$AzoC$_5$N$^+$/clay single nanosheets/ Prussian Blue) [13–15].

Floating hybrid monolayers at the air–suspension interface and their transfer process

The π–A isotherms was measured to investigate the state of floating hybrid monolayers at the air–suspension interface (Fig. 3). As can be seen, it appears that the lift-off area in the π–A isotherms of floating hybrid monolayers on clay suspension tends to shift toward larger areas as the concentration of the clay suspension increases. This trend indicates that charged C$_{12}$AzoC$_5$N$^+$ monolayers could be electrostatically adsorbed onto the clay single nanosheets at the air-suspension interface. Briefly, the shift in the lift-off area on the isotherms is corresponding to changes in the density of amphiphiles at the air–suspension interface [34–35]. In the case of this work, as already described above, the lift-off area on the isotherms shifted toward larger areas as the clay concentration in the suspension increases. In other words, it is supposed that the density of C$_{12}$AzoC$_5$N$^+$ is small in floating hybrid monolyers prepared at higher clay concentration in the suspension. The lowering of C$_{12}$AzoC$_5$N$^+$ density is caused by the fact that, due to the high clay concentration in the suspension, the floating hybrid monolayers are almost immediately formed at the air–suspension interface before C$_{12}$AzoC$_5$N$^+$ themselves aggregate to form monolayer domains. It is remarkable that the π–A isotherm of floating hybrid monolayers on the clay suspension of 50 mg l^{-1} showed the formation of stable hybrid monolayers at the air–suspension interface and hence, the transfer of the floating hybrid monolayers was carried out under the condition as follows: the clay suspension of 50 mg l^{-1}, the transfer at 30 mN m^{-1}.
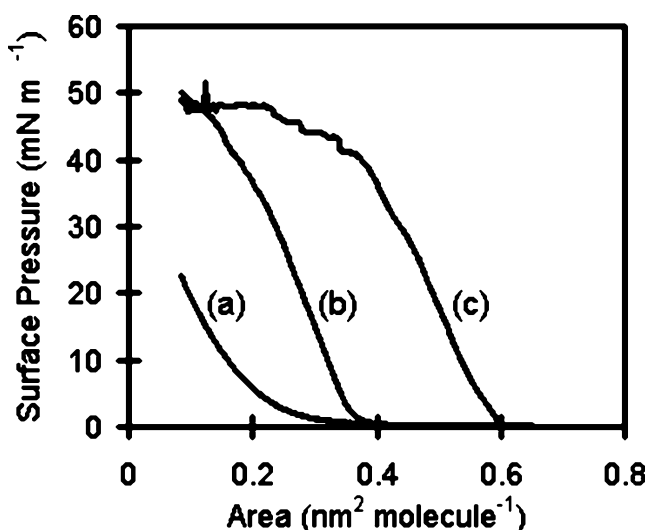
Fig. 3 π–A isotherm curves for floating monolayers of C$_{12}$AzoC$_5$N$^+$ on **a** pure water and on the clay suspensions at **b** 50 and **c** 100 mg l^{-1}

The formation of the hybrid ultrathin film was monitored by UV–vis absorption spectra measured in the process of the film preparation at room temperature. Each spectrum gave two intense absorption peaks at 370 nm and around 700 nm. The peak at 370 nm is ascribed to the π–π* transition of the *trans*-C$_{12}$AzoC$_5$N$^+$ and the peak at around 700 nm is related to the intervalence charge transfer (IVCT) band from Fe^{II} to Fe^{III} in Prussian Blue. To confirm a reproducible transfer of floating hybrid monolayers, the absorbance of the π–π* transition of C$_{12}$AzoC$_5$N$^+$ was plotted as a function of the layer number. As a result, a linear increase in the absorbance could be seen, which indicates a reproducible transfer of floating monolayers in a layer-by-layer manner. Similarly, successive formation of Prussian Blue onto the clay layer was monitored by plotting the absorbance of IVCT band vs. layer number. Consequently, a linear increase in absorbance was seen and hence, the adsorption process of Prussian Blue was also reproducible.

Structures of the hybrid ultrathin film

To determine the orientation of C$_{12}$AzoC$_5$N$^+$ in the hybrid ultrathin film, p-polarized IR-ER spectra were measured with varying the incident angle. These spectra gave two absorption peaks at 2914 and 2847 cm^{-1}, which are assigned to the antisymmetric and symmetric CH$_2$ stretching [$\nu_{(a)}$(CH$_2$) and $\nu_{(s)}$(CH$_2$)] vibrations of C$_{12}$AzoC$_5$N$^+$, respectively. The reflection absorbance for the $\nu_{(a)}$(CH$_2$) and $\nu_{(s)}$(CH$_2$) band was plotted as a function of the incident angle. Consequently, the peaks due to both bands appear as the negative absorbance below the Brewster angle and, on the other hand, the same peaks appear as the positive one in the spectra with the incident angle above the Brewster angle. These spectral data indicate that the transition moments of the $\nu_{(a)}$(CH$_2$) and $\nu_{(s)}$(CH$_2$) band are estimated to be parallel to the film surface, that is, the alkyl chain of C$_{12}$AzoC$_5$N$^+$ in the hybrid ultrathin film are almost perpendicular to the layers.

The XRD pattern (θ–2θ mode) for the hybrid ultrathin film gave six diffraction peaks at 2θ = 2.70, 6.18, 9.82, 14.1, 17.6, and 22.1 ° (Fig. 4). These peaks are corresponding to the (001), (002), (003), (004), and (005) reflections of the clay layer, respectively. Thus, the hybrid ultrathin film obviously possesses the layered structure, and from the (001) diffraction peak, the basal spacing of the unit layer (C$_{12}$AzoC$_5$N$^+$/clay single nanosheets/Prussian Blue) is calculated to be 32.7 Å. Based on the p-polarized IR-ER results, the alkyl chains of the C$_{12}$AzoC$_5$N$^+$ is almost perpendicular to the film surface, and the thickness of the clay single nanosheets is known (9.6 Å) [37], the thickness of the adsorbed Prussian Blue layers (–CN–Fe–NC–Fe–O) is determined to be 6.0 Å. On this occasion, it is
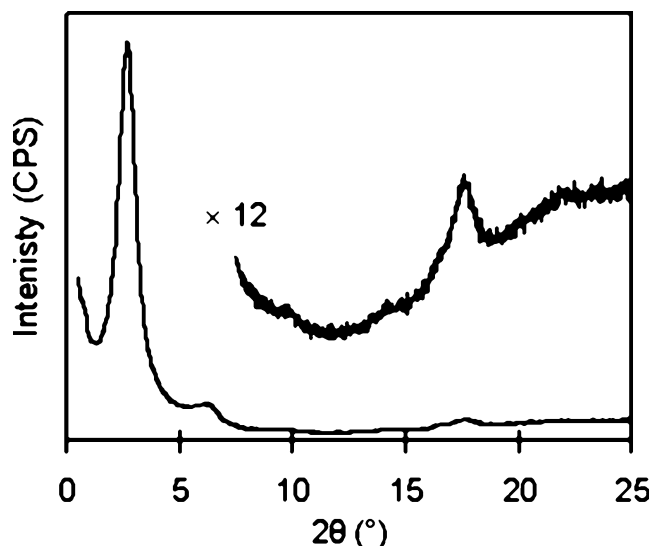
Fig. 4 XRD patterns (θ–2θ mode) for film A

suggested that roughly single layer (a half of the unit cell) of the three-dimensional Prussian Blue lattice is formed.

Photoisomerization of $C_{12}AzoC_5N^+$ in the hybrid ultrathin film

Photoisomerization of $C_{12}AzoC_5N^+$ in the hybrid ultrathin film was monitored by UV–vis absorption spectra. The UV–vis spectral changes due to photoisomerization at room temperature are shown in Fig. 5. UV illumination resulted from the decrease of the absorbance at 370 nm ascribed to the π–π^* transitions of the *trans*-$C_{12}AzoC_5N^+$, which indicates that *trans*-to-*cis* isomerization occurred in the hybrid ultrathin film. Moreover, the fraction of *cis*-$C_{12}AzoC_5N^+$ at the photostationary state was estimated to be ca. 45% by using a calculation based on the difference spectra [38]. This lower conversion compared to the solution system is because the photoisomerization of azobenzene derivatives, particularly *trans*-to-*cis* isomerization, is accompanied by an increase in the molecular volume. After subsequent illumination with visible light, the reverse process (i.e. *cis*-to-*trans* isomerization) also proceeded to a certain degree. The overall *trans*–*cis* isomerization cycle was repeated between the two photostationary states. Similar spectral changes were also observed in the measurements at 10 K.

Magnetic properties of the hybrid ultrathin film

The field cooled magnetization (FCM) plots with an applied magnetic field of 10 G for the hybrid ultrathin film exhibits ferromagnetic transition at a critical temperature (T_C) of 3.2 K. This lower T_c value than that of the bulk Prussian Blue (5.6 K) [39] indicates that the number of

exchange pathways per magnetic ion is reduced due to lowering structural coherence or the dimensions. In addition, the presence of a ferromagnetic interaction at low temperature was supported by the plot of the magnetization as a function of an applied magnetic field at 2 K, where a magnetic hysteresis loop was observed.

Subsequently, we investigated the influence of light illumination on the magnetic properties of the hybrid ultrathin film and also determined how the magnetization changed by alternate illumination with UV and visible light at 2 K (Fig. 6). After the UV light illumination the magnetization value decreased and the subsequent illumination with visible light led to recovery of the magnetization. After this process, the UV light-induced decrease and the visible light-induced increase of the magnetization were repeated several times. The total photoinduced changes in the magnetization values are estimated to be ca. 11%. As already mentioned, the absorption maximum (λ_{max}) of the IVCT band for the hybrid ultrathin film was observed at around 700 nm. Figure 7 shows the changes in the λ_{max} before and after the alternating photoillumination. After UV illumination, the λ_{max} was red-shifted from 720 to 739 nm. On the other hand, after visible light illumination, the λ_{max} was blue-shifted from 739 to 720 nm. It is noteworthy that this reversible change is almost consistent with the changes in the magnetization (Fig. 6). It is proposed that changes in the electrostatic field driven by the photoisomerization of the azobenzene chromophore brought about changes in the Coulombic energy within the Prussian Blue layer, which is necessary to transfer an electron from the $[Fe^{II}(CN)_6]^{4-}$ ion to Fe^{III} species, and this
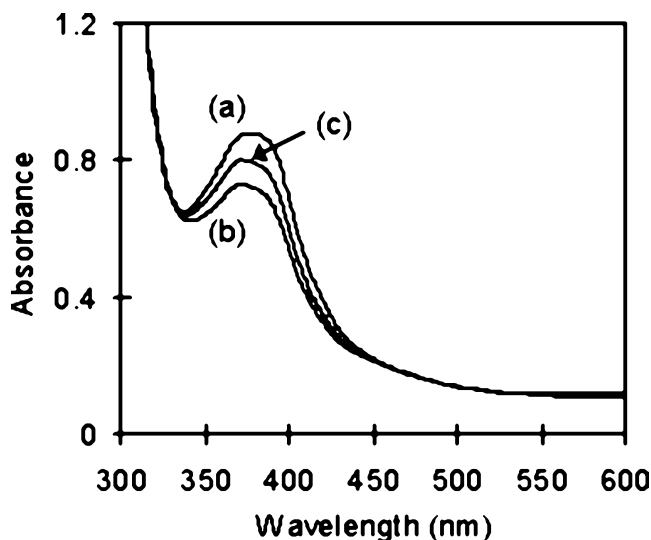

Fig. 5 Changes in the UV–vis absorption spectra for film A upon photoillumination at room temperature: **a** initial state, **b** after UV illumination (the *cis*-rich photostationary state), and **c** subsequent illumination with visible light (the *trans*-rich photostationary state). After this process, the photoisomerization cycle was repeated between the spectra **b** and **c** several times

might affect the superexchange interaction between the spins in the Prussian Blue.

In summary, we have succeeded in designing the photomagnetic ultrathin film on the basis of our proposed strategy, i.e. the incorporation of magnetic materials into photochromic assemblies. Photocontrol in the magnetization was realized by the photoisomerization of azobenzene chromophores, in which the observed photomagnetic efficiency was large (ca. 11%) due to the formation of the layered structure. It is noted that Prussian Blue itself is not photoresponsive and hence the photomagnetic property of Film A is truly derived from the photoisomerization of azobenzenes.

Section for Film B (DDAB/clay single nanosheets/Co–Fe Prussian Blue) [40, 41].

Floating hybrid monolayers at the air–suspension interface and their transfer process

The π–A isotherms was measured to investigate the state of floating hybrid monolayers at the air–suspension interface (Fig. 8). As seen in the figure, it appears that the lift-off area in the π–A isotherms of floating hybrid monolayers on the clay suspension tends to shift toward larger areas as the concentration of the clay suspension increases as seen in the above section. This trend again indicates that charged DDAB monolayers could be electrostatically adsorbed onto the clay single nanosheets at the air–suspension interface. Therefore, the transfer of the floating hybrid monolayers was carried out under the condition as follows: clay suspension of 90 mg l^{-1}; transfer at 10 mN m^{-1}.
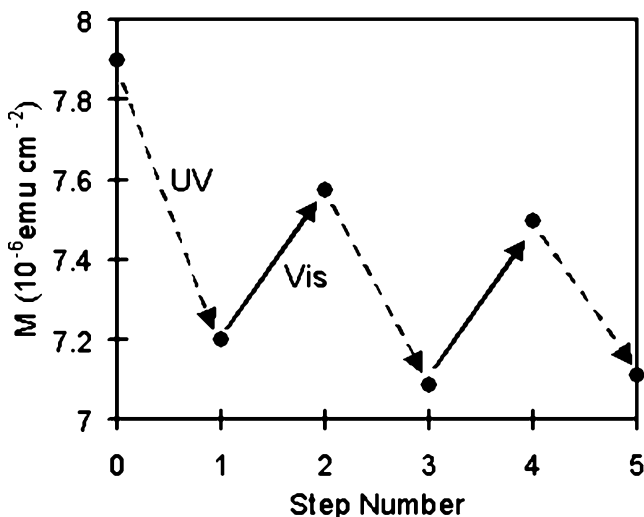
Fig. 6 Changes in the magnetization for film A upon photoillumination at 2 K with an applied magnetic field of 10 G. In UV cycles (i.e., from step number 0 to 1, 2 to 3, and 4 to 5), film A was illuminated with UV light. On the other hand, in vis cycles (i.e., from step number 1 to 2 and 3 to 4), film A was illuminated with visible light
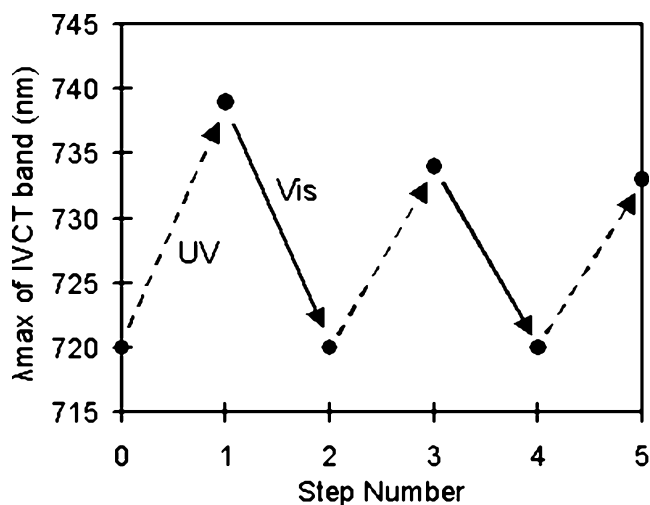

Fig. 7 Relationships between photoisomerization cycle and changes in the absorption maximum (λ_{max}) of the IVCT band for film A at room temperature. In UV cycles (i.e., from step number 0 to 1, 2 to 3, and 4 to 5), film A was illuminated with UV light. On the other hand, in vis cycles (i.e., from step number 1 to 2 and 3 to 4), film A was illuminated with visible light

The formation of hybrid ultrathin film was monitored by FT-IR absorption spectra measured in the process of film preparation at room temperature. Each spectrum gave some characteristic stretching vibration bands: CH$_3$ antisymmetric (at 2957 cm^{-1}), CH$_2$ antisymmetric (at 2925 cm^{-1}) and symmetric (at 2848 cm^{-1}), and CN bridging (at 2159 cm^{-1} for Fe^{III}–CN–Co^{II} and at 2094 cm^{-1} for Fe^{II}–CN–Co^{II}). To confirm a reproducible transfer of hybrid monolayers, the absorbance of CH$_2$ antisymmetric and symmetric vibration was respectively plotted as a function of the layer number. As results, each absorbance increased regularly as the layer number increased. Therefore, the transfer of hybrid monolayers was proceeded successfully. The successive formation of Co–Fe Prussian Blue onto the clay layer was similarly monitored by plotting the absorbance of CN stretching vibration vs. layer number. As a consequence, a regular increase in absorbance was also seen and, hence, the adsorption process of Co–Fe Prussian Blue was also reproducible.

Structure of the hybrid ultrathin film

To determine the structure of hybrid ultrathin film, we performed XRD measurements in both θ–2θ and in-plane mode. Figure 9a shows the XRD pattern obtained in a θ–2θ mode measurement and, as can be seen, five diffraction peaks were given at 2θ=3.94 °, 7.87 °, 16.1 °, 19.9 °, and 24.5 °. These peaks are ascribed to the (001), (002), (004), (005), and (006) reflections of the clay layer, respectively. Thus, the hybrid ultrathin film obviously possesses the layered structure and, from the (001) diffraction peak, the
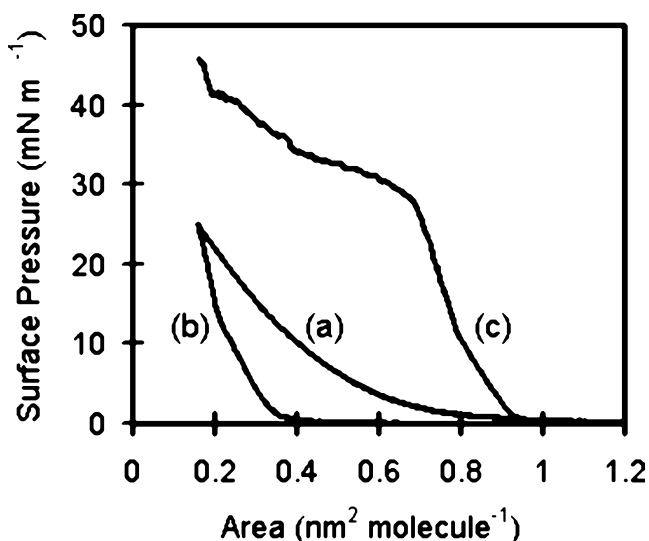
Fig. 8 π–A isotherm curves for floating monolayers of DDAB on **a** pure water and on the clay suspensions at **b** 20 and **c** 90 mg l^{-1}

basal spacing of the unit layer (DDAB/clay single nanosheets/Co–Fe Prussian Blue) is calculated to be 22.4 Å. According to the result of p-polarized IR-ER measurements for film A, the alkyl chains of the amphiphile are almost perpendicular to the film surface. Therefore, it is supposed that the alkyl chains of DDAB are almost perpendicular to the film surface. Taking this estimation into account, the thickness of the adsorbed Co–Fe Prussian Blue layers (–NC–Fe–CN–Co–O) is calculated to be 4.0 Å. In this case, also similar to the case of film A, roughly a single layer (a half of the unit cell) of Co–Fe Prussian Blue network would be formed in the hybrid ultrathin film.

An in-plane XRD measurement was subsequently performed to verify the presence of in-plane structural correlations in the hybrid ultrathin film. As a result, four diffraction peaks were given at 2θ =17.6 °, 19.8 °, 25.1 °, and 35.0 ° (Fig. 9b). Peaks at 2θ =17.4 ° and 25.1 ° are corresponding to the (200) and (220) Bragg reflections at d spacings of 5.10 and 3.55 Å, respectively, from a face-centered square cell of a=10.2 Å for the Co–Fe Prussian

Blue structure [42], and those at 2θ=19.8 ° and 35.0 ° are assignable to the (110) and (020), and (130) reflections of the clay layer [43]. From this result, it is indicated that the adsorbed Co–Fe Prussian Blue layer forms the ordered structure along the film surface plane. Moreover, an analysis of the (200) peak width by application of the Scherrer equation [44] yields an average crystalline coherence length of ~160 Å or a 16-unit cell length.

Photoinduced electron transfer in the hybrid ultrathin film at low temperature and its relaxation process

As firstly reported by Sato et al. [8], upon red light illumination, the electron transfer from Fe^{II} to Co^{III} through CN group occurred at low temperature. As a result, the oxidation state changed into Fe^{III} (LS, S=1/2)–CN–Co^{II} (HS, S=3/2) from Fe^{II} (LS, S=0)–CN–Co^{III} (LS, S=0), where HS and LS represent high spin and low spin, respectively. This photoinduced electron transfer process has been mainly discussed by monitoring changes in the FT-IR absorption spectra (CN bridging mode) at low temperature.

Firstly, FT-IR absorption spectrum was measured at 300 and 8 K. At 300 K, almost cobalt ions exist as the high-spin state: the main absorption peak located at 2094 cm^{-1}. On the contrary, at 8 K, the spin state of cobalt ions changes into the low spin: the peak broadened and its center shifted to 2112 cm^{-1}. We subsequently examined the photoinduced electron transfer upon illumination with visible light and the result was shown in Fig. 10. Before illumination, the broad peak centered at 2112 cm^{-1} was observed, which is ascribed to the CN stretching vibration Fe^{II} (LS, S=0)–CN–Co^{III} (LS, S=0). Upon visible light illumination, the peak separated into the two peaks located at 2163 and 2092 cm^{-1}, attributed to the CN bridging mode of Fe^{III} (LS, S=1/2)–CN–Co^{II} (HS, S=3/2) and Fe^{II} (LS, S=0)–CN–Co^{III} (LS, S=0), respectively. Thus, the photoinduced electron transfer was realized even in the hybrid ultrathin films prepared herein.

**Fig. 9** XRD patterns for film B: **a** θ–2θ mode and **b** in-plane mode
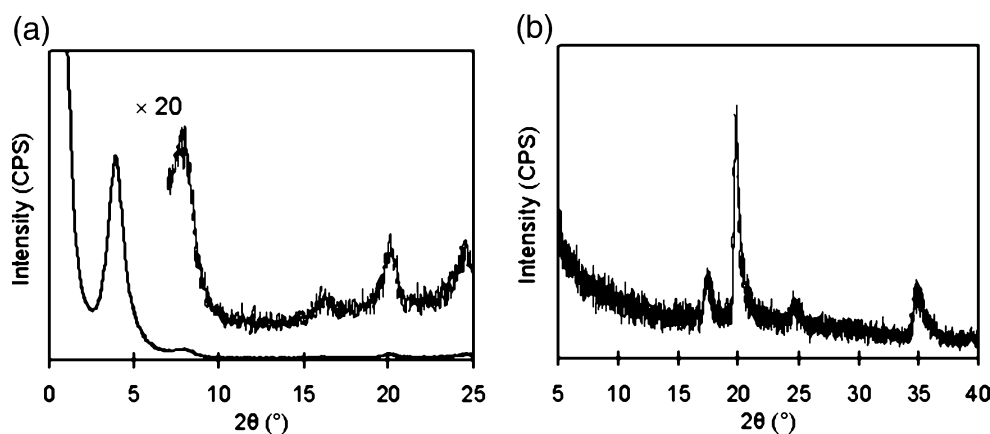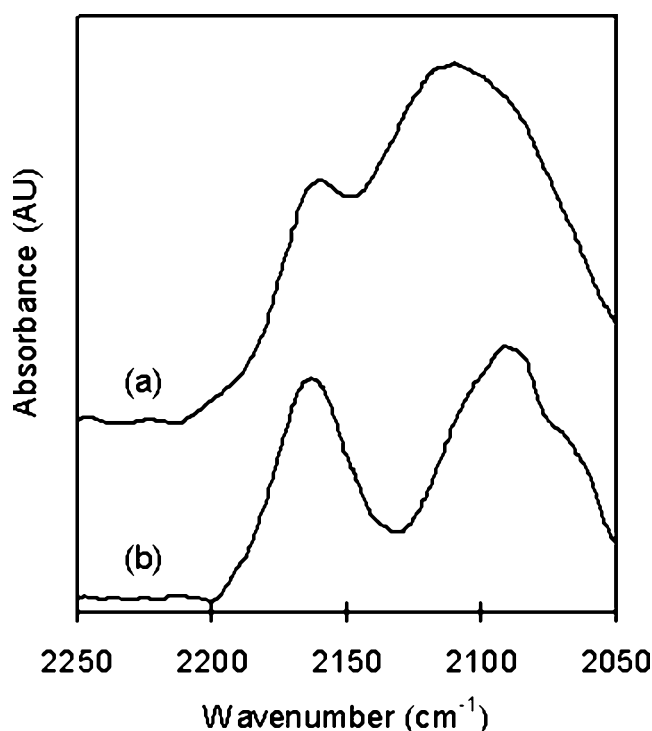
Fig. 10 Changes in the FT–IR spectra for film B upon photo-illumination at 8 K: **a** initial state and **b** after visible light illumination at 8 K

It has been reported that the generated HS state relaxed into the initial state by annealing above 150 K [45]. To confirm the relaxation temperature, we measured the temperature dependence of the FT-IR absorption spectrum. Upon heating, the peak at 2163 cm^{-1} decreased and, in contrast, the peak at 2092 cm^{-1} increased. As the temperature reached at 160 K, the peak at 2092 cm^{-1} shifted towards higher wavenumber and broadened. In other words, CN bridging mode returned to its initial state: Fe^{II} (LS, $S=0$)–CN–Co^{III} (LS, $S=0$). It was also observed that further heating led to the enhancement of this peak. In this sense, the electron transfer from Co^{II} (HS, $S=3/2$) species back to Fe^{III} (LS, $S=1/2$) ones is thermally induced.
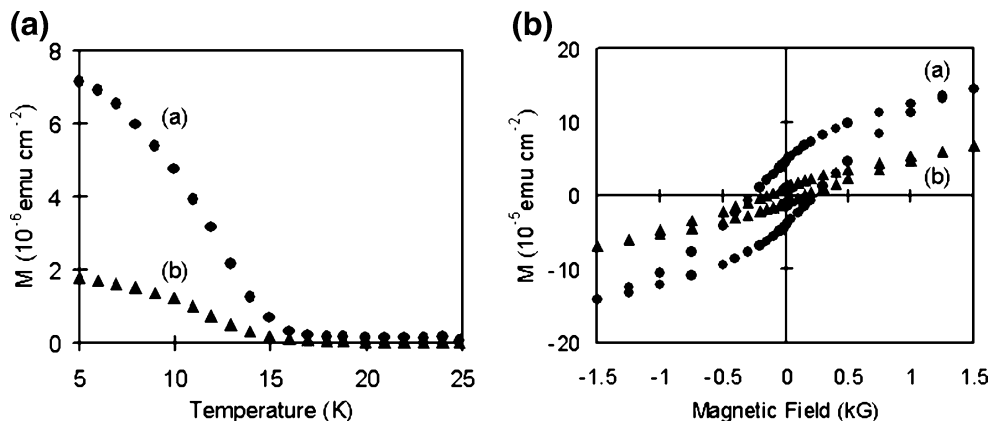
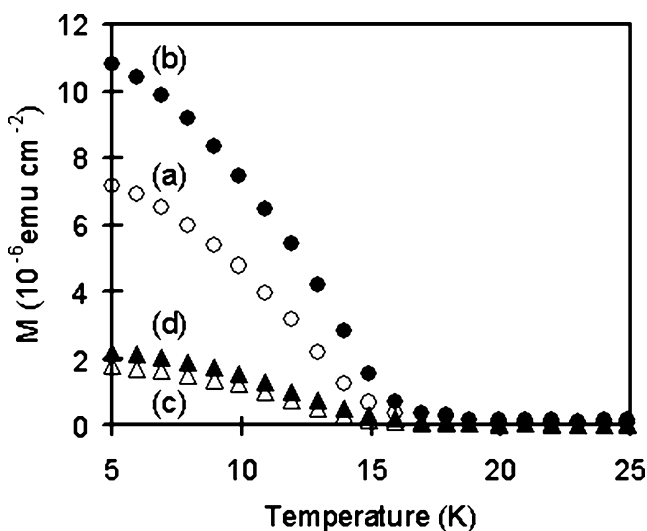## Magnetic properties of the hybrid ultrathin film

The FCM plots with an applied magnetic field of 10 G for the hybrid ultrathin film exhibits ferrimagnetic transition at a critical temperature (T_C) of 14 K (Fig. 11a). In addition, the hybrid ultrathin film clearly exhibits the magnetic anisotropy due to the low-dimensional structure of the Co–Fe Prussian Blue layer. In detail, when the film surface was oriented parallel to the applied magnetic field, the observed magnetization values were higher than the film surface oriented perpendicular to the magnetic field. The presence of a ferrimagnetic state at low temperature is further supported by the dependence of the magnetization on the applied magnetic field data taken at 5 K. As a result, cycling the magnetic field at 5 K resulted in the hysteresis loops (Fig. 11b). There is again clear anisotropy in the magnetic behavior between the two orientations of the sample with regard to the magnetic field. When the magnetic field is parallel to the sample surface, the magnetization increases more rapidly with respect to the field and the coercive field is also slightly anisotropic, being 250 G in parallel orientation and 150 G in the perpendicular orientation.

We subsequently investigated the photoinduced magnetization effect of the Co–Fe Prussian Blue in hybrid ultrathin film. Light illumination was performed at 5 K with an applied magnetic field of 10 G and the wavelength of the light was 400–700 nm. The influence on the magnetization upon light illumination was examined in both orientations with regard to the applied magnetic field (the parallel and perpendicular orientation). Figure 12 demonstrates the results in changes in the magnetization upon light illumination. As seen in the figure, the photoinduced magnetization effect was observed in both orientations. However, the degree of increase in the magnetization was different in the direction of the applied magnetic field. In this sense, the photoinduced magnetization effect was also interestingly anisotropic. The magnetization increases much more intensely when the magnetic field is parallel to the sample surface, and the changes in the magnetization is 60 vs 10% in the perpendicular orientation.

Fig. 11 **a** Temperature dependence of the magnetization for film B after field cooling in 10 G: (*a*) the sample surface aligned parallel to the applied magnetic field and (*b*) the sample surface aligned perpendicular to the magnetic field. **b** Hysteresis loops for film B measured at 5 K: (*a*) the sample surface aligned parallel to the applied magnetic field and (*b*) the sample surface aligned perpendicular to the magnetic field

Fig. 12 Temperature dependence of the magnetization for film B before and after visible light illumination at 5 K: **a** initial state in parallel orientation to the magnetic field, **b** photoinduced state in parallel orientation to the magnetic field, **c** initial state in perpendicular orientation to the magnetic field, and **d** photoinduced state in perpendicular orientation to the magnetic field

Such an "anisotropic photoinduced magnetization effect" would be closely related to the dipolar magnetic field generated by the ferrimagnetic domain with the structure of Co–Fe Prussian Blue. That is, if the Co–Fe Prussian Blue forms the two-dimensional network (i.e., ultrathin sheets) in the hybrid ultrathin film, the generated dipolar magnetic field would be maximized. As a consequence, the net magnetization of the films in the photoinduced state should decrease when the film surface was oriented perpendicular to the applied magnetic field. Taking this information into account, it is deduced that the each coherent Co–Fe Prussian Blue network in the hybrid ultrathin film would not be linked and separated from each other with an isolated wire- or rod-like structure (Fig. 13). In other words, Co–Fe Prussian Blue does not form a "perfect" two-dimensional grid network. In this case, the generated dipolar field would be minimized and, hence, the net magnetic field acting on Co–Fe Prussian Blue is nearly equal to the applied magnetic field. Therefore, in spite of the generation of "perfect" species by the photoinduced electron transfer from Fe^{II} to Co^{III}, the resultant increase of the spin values was not reflected in the magnetization values due to the existence of magnetic anisotropy in the hybrid ultrathin film. Thus, the degree of the photoinduced magnetization is consistent with that of the magnetization before light illumination.

In summary, we have fabricated the unique Co–Fe Prussian Blue network by using hybrid monolayers (DDAB and clay single nanosheets) as a template. This hybrid ultrathin film also possesses the layered structure and, moreover, the crystalline coherent length of the Co–Fe

Prussian Blue network was estimated to be 160 Å. The photoinduced magnetization effect exhibited an anisotropic response with regards to the direction of the applied magnetic field, which is ascribed to the formation of the one-dimensional Co–Fe Prussian Blue network. It is emphasized that such an anisotropic response in the photoinduced magnetization effect has not been observed in the bulk Co–Fe Prussian Blue.

Conclusions

We have described two novel types of photomagnetic hybrid ultrathin film (films A and B) of metal cyanides. These photomagnetic ultrathin films have been fabricated by means of the modified Langmuir–Blodgett technique using a smectite clay mineral. Film A (azobenzenes/clay single nanosheets/Prussian Blue) was designed on the basis of our proposed strategy, i.e., the incorporation of magnetic materials into photochromic assemblies. Photocontrol in the magnetization was realized by the photoisomerization of azobenzene chromophores, in which the observed photomagnetic efficiency was large (ca. 11%) due to the formation of the layered structure. It is noted that Prussian Blue itself is not photoresponsive and hence the photomagnetic property of film A is truly derived from the photoisomerization of azobenzenes. Moreover, such a multi-component photofunctional ultrathin film would be difficult to prepare by conventional methods. As for film B (ammonium salts/clay single nanosheets/Co–Fe Prussian Blue), hybrid monolayers composed of ammonium salts and clay single nanosheets play a template role for the formation of the Co–Fe Prussian Blue layer. Film B also possesses the layered structure and, moreover, the crystalline coherent length of the Co–Fe Prussian Blue network was estimated to be 160 Å. The photoinduced magnetiza-
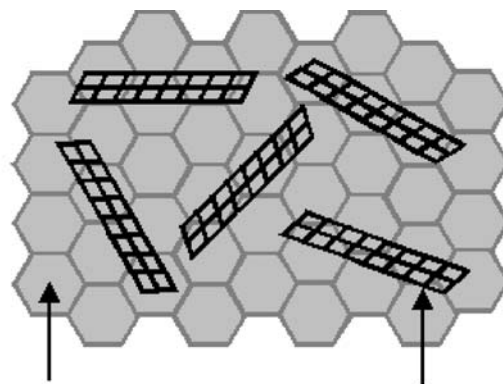
Fig. 13 Deduced structure of the Co–Fe Prussian Blue network in film B (top view)

tion effect exhibited an anisotropic response with regards to the direction of the applied magnetic field. This phenomenon is ascribed to the unique one-dimensional structure of Co–Fe Prussian Blue formed onto the clay layer. It is emphasized that such an anisotropic response in the photoinduced magnetization effect has not been observed in the bulk Co–Fe Prussian Blue.

The present work demonstrates the successful and effective methodology for fabricating photomagnetic ultrathin films. In addition, this work will offer new prospects not only for the development of photofunctional ultrathin films but also for future applications to nanoscale magnetic devices, which are currently attracting much interest in the high-density magnetic recording system.

References

1. Kuch W (2003) Nat Mater 2:505
2. Thirion C, Wernsdorfer W, Mailly D (2003) Nat Mater 2:524
3. Gütlich P, Garcia Y, Woike T (2001) Coord Chem Rev 219–221:839
4. Sato O, Hayami S, Einaga Y, Gu Z (2003) Bull Chem Soc Jpn 76:443
5. Sato O (2004) J Photochem Photobiol C 5:203
6. Bousseksou A, Molnar G, Matouzenko G (2004) Eur J Inorg Chem 4353
7. Matsuda K (2005) Bull Chem Soc Jpn 78:383
8. Sato O, Iyoda T, Fujishima A, Hashimoto K (1996) Science 272:704
9. Li G, Akitsu T, Sato O, Einaga Y (2003) J Am Chem Soc 125:12396
10. Hayami S, Gu Z, Shiro M, Einaga Y, Fujishima A, Sato O (2000) J Am Chem Soc 122:7126
11. Einaga Y, Sato O, Iyoda T, Fujishima A, Hashimoto K (1999) J Am Chem Soc 121:3745
12. Einaga Y, Yamamoto T, Sugai T, Sato O (2002) Chem Mater 14:4846
13. Yamamoto T, Umemura Y, Sato O, Einaga Y (2004) Chem Mater 16:1195
14. Yamamoto T, Murofushi A, Umemura Y, Sato O, Einaga Y (2004) Trans Mater Res Soc Jpn 29:885
15. Yamamoto T, Umemura Y, Sato O, Einaga Y (2006) Sci Technol Adv Mater 7:134
16. Taguchi M, Yamada K, Suzuki K, Sato O, Einaga Y (2005) Chem Mater 17:4554
17. Einaga Y, Taguchi M, Li G, Akitsu T, Gu Z, Sugai T, Sato O (2003) Chem Mater 15:8
18. Taguchi M, Li G, Gu Z, Sato O, Einaga Y (2003) Chem Mater 15:4756
19. Mikami R, Taguchi M, Yamada K, Suzuki K, Sato O, Einaga Y (2004) Angew Chem Int Ed 43:6135
20. Suda M, Miyazaki Y, Hagiwara Y, Sato O, Shiratori S, Einaga Y (2005) Chem Lett 34:1028
21. Benard S, Riviere E, Yu P, Nakatani K, Delouis F (2001) Chem Mater 13:159
22. Benard S, Leaustic A, Riviere E, Yu P, Clement R (2001) Chem Mater 13:3709
23. Okubo M, Enomoto M, Kojima N (2005) Solid State Commun 134:777
24. Ulman A (1991) An introduction to ultrathin organic films: from Langmuir–Blodgett to self-assembly. Academic, San Diego
25. Petty MC (1996) Langmuir–Blodgett films: an introduction. Cambridge University Press, Cambridge
26. Ulman A (1996) Chem Rev 96:1533
27. Mallouk TE, Gavin JA (1998) Acc Chem Res 31:209
28. Sato O, Einaga Y, Iyoda T, Fujishima A, Hashimoto K (1997) J Electrochem Soc 144:L11
29. Ohkoshi S, Einaga Y, Fujishima A, Hashimoto K (1999) J Electroanal Chem 473:245
30. Hozumi T, Hashimoto K, Ohkoshi S (2005) J Am Chem Soc 127:3864
31. Culp JT, Park J, Stratakis D, Meisel MW, Talham DR (2002) J Am Chem Soc 124:10083
32. Torres GR, Agricole B, Mingotaud C, Ravaine S, Delhaes P (2003) Langmuir 19:4688
33. Tamura K, Setsuda H, Taniguchi M, Yamagishi A (1999) Langmuir 15:6915
34. Umemura Y, Yamagishi A, Schoonheydt R, Persoons A, De Schryber F (2001) Langmuir 17:449
35. Umemura Y, Yamagishi A, Schoonheydt R, Persoons A, De Schryber F (2002) J Am Chem Soc 124:992
36. Shimonura M, Ando R, Kunitake T (1983) Ber Bunsen-Ges Phys Chem 87:1134
37. Moore DM, Reynolds RC Jr (1997) X-ray diffraction and the identification and analysis of clay minerals. Oxford University Press, New York
38. Brode WR, Gould JH, Wyman GM (1952) J Am Chem Soc 74:4641
39. Herren F, Fischer P, Ludi A, Hälg W (1980) Inorg Chem 19:956
40. Yamamoto T, Umemura Y, Sato O, Einaga Y (2004) Chem Lett 33:500
41. Yamamoto T, Umemura Y, Sato O, Einaga Y (2005) J Am Chem Soc 127:16065
42. Ludi A, Gudel HU (1973) Struct Bond 14:1
43. Takahashi S, Taniguchi M, Omote K, Wakabayashi N, Tanaka R, Yamagishi A (2002) Chem Phys Lett 352:213
44. Guinaier A (1968) X-ray diffraction. Freeman, San Fransisco
45. Sato O, Einaga Y, Fujishima A, Hashimoto K (1999) Inorg Chem 38:4405